

1 **Revisiting the Austral Spring Extratropical Southern**  
2 **Hemisphere zonally asymmetric circulation using**  
3 **complex Empirical Orthogonal Functions**

4 **Elio Campitelli · Leandro B. Díaz ·**  
5 **Carolina Vera ·**

6  
7 Received: date / Accepted: date

8 **Abstract** abstract  
9

10 **Keywords** ·

---

The research was supported by UBACyT20020170100428BA and the CLIMAX Project funded by Belmont Forum/ANR-15-JCL/-0002-01. Elio Campitelli was supported by a PhD grant from CONICET, Argentina.

Elio Campitelli

Universidad de Buenos Aires, Facultad de Ciencias Exactas y Naturales, Departamento de Ciencias de la Atmósfera y los Océanos. Buenos Aires, Argentina.

CONICET – Universidad de Buenos Aires. Centro de Investigaciones del Mar y la Atmósfera (CIMA). Buenos Aires, Argentina.

CNRS – IRD – CONICET – UBA. Instituto Franco-Argentino para el Estudio del Clima y sus Impactos (IRL 3351 IFAECI). Buenos Aires, Argentina.

E-mail: [elio.campitelli@cima.fcen.uba.ar](mailto:elio.campitelli@cima.fcen.uba.ar)

Leandro B. Díaz

Universidad de Buenos Aires, Facultad de Ciencias Exactas y Naturales, Departamento de Ciencias de la Atmósfera y los Océanos. Buenos Aires, Argentina. CONICET – Universidad de Buenos Aires. Centro de Investigaciones del Mar y la Atmósfera (CIMA). Buenos Aires, Argentina. CNRS – IRD – CONICET – UBA. Instituto Franco-Argentino para el Estudio del Clima y sus Impactos (IRL 3351 IFAECI). Buenos Aires, Argentina.

Argentina. CNRS – IRD – CONICET – UBA. Instituto Franco-Argentino para el Estudio del Clima y sus Impactos (IRL 3351 IFAECI). Buenos Aires, Argentina.

Carolina Vera

Universidad de Buenos Aires, Facultad de Ciencias Exactas y Naturales, Departamento de Ciencias de la Atmósfera y los Océanos. Buenos Aires, Argentina. CONICET – Universidad de Buenos Aires. Centro de Investigaciones del Mar y la Atmósfera (CIMA). Buenos Aires, Argentina. CNRS – IRD – CONICET – UBA. Instituto Franco-Argentino para el Estudio del Clima y sus Impactos (IRL 3351 IFAECI). Buenos Aires, Argentina.

Argentina. CNRS – IRD – CONICET – UBA. Instituto Franco-Argentino para el Estudio del Clima y sus Impactos (IRL 3351 IFAECI). Buenos Aires, Argentina.

## 1 Introduction

introduction

The large-scale extratropical circulation in the Southern Hemisphere (SH) is strongly zonally symmetric, but its zonal departures are highly relevant for regional impacts (e.g. Hoskins and Hodges 2005). They strongly modulate weather systems and regional climate through promoting longitudinally different latitudinal transport of heat, humidity, and momentum (K. E. Trenberth 1980; M. N. Raphael 2007) and could even be related to the occurrence of high-impact climate extremes (Pezza, Rashid, and Simmonds 2012).

Zonally asymmetric circulation is typically described by the amplitude and phase of zonal waves obtained by Fourier decomposition of geopotential heights or sea-level pressures at each latitude (e.g. van Loon and Jenne 1972; K. E. Trenberth 1980; Turner et al. 2017). This approach suggests that zonal waves 1 and 3 explain almost 99% of the total variance in the annual mean 500-hPa pattern at 50°S (van Loon and Jenne 1972). K. F. Trenberth and Mo (1985) concluded that wave 3 plays a role in the development of blocking events. In addition, previous works have identified at extratropical and subpolar latitudes, wave-like patterns with dominant wavenumbers 3-4, also exerting distinctive regional impacts. M. N. Raphael (2007) shows that variability in the planetary wave 3 projected onto its climatological location is associated with anomalies in the Antarctic sea-ice concentration.

The Fourier decomposition relies on the assumption that the circulation can be meaningfully described in terms of zonal waves of constant amplitude along a latitude circle. However, this is not valid for meridionally propagating waves or zonal waves with localised amplitudes. Addressing this limitation, the Fourier technique can be generalized to integrate all planetary wave amplitude regardless of wave number, by computing the wave envelope (Irving and Simmonds 2015). The latter makes it possible to represent planetary waves with different amplitude at different longitudes, but it removes all information about phase and wave number. With this approach, Irving and Simmonds (2015) showed that planetary wave amplitude in general is associated to Antarctic sea-ice concentration and temperature, as well as to precipitation anomalies in regions of significant topography in SH mid-latitudes and Antarctica.

Another extensively used approach to characterize the SH tropospheric circulation anomalies, is by computing Empirical Orthogonal Functions (EOF, also known as Principal Component Analysis). Within the EOF framework, the Southern Annular Mode (SAM) appears as the leading mode of variability of the SH circulation (Fogt and Marshall 2020). SAM represents a relatively zonally symmetric pattern of alternating low pressures in polar latitude and a ring of high pressures in high latitudes with an embedded wave 3 pattern that is more prominent in the Pacific sector. The 2nd and 3rd EOFs, usually known as Pacific-South American Patterns (PSA) 1 and PSA2 patterns, respectively, describe meridionally propagating wave trains that originate in the eastern equatorial Pacific and Australian-Indian Ocean sector, and travel towards the South Atlantic following a great-circle arch along the Antarctic

coast (Mo and Paegle 2001). These patterns influence precipitation anomalies in South America (Mo and Paegle 2001). Although these patterns are usually derived by applying EOF to temporal anomalies, (M. Raphael 2003) also applied EOF methods specifically to zonal anomalies. More recently, (Irving and Simmonds 2016) proposed a novel methodology for objectively identifying the PSA pattern using Fourier decomposition.

Patterns resulting from EOF analyses are more flexible than Fourier decomposition derived modes in the sense that they can capture oscillation patterns that cannot be characterised by purely sinusoidal waves with constant amplitude. Nonetheless, they are restricted to standing oscillation modes and could not represent properly propagating or phase-varying features such as zonal waves. A single EOF can also represent a mixture of two or more physical modes.

A third methodology commonly used consists on identifying particular features of interest and creating indices using simple methods such as averages and differences. Examples of this methodology are the SAM Index of (Gong and Wang 1999), the SH wave 3 activity index defined by M. N. Raphael (2004) and the SH zonally asymmetric circulation index from Hobbs and Raphael (2010). These derived methods are grounded on other methods such as Fourier decomposition or EOF to identify the centres of action for the described phenomena and can be useful to characterise features that are not readily apparent with these methods. It is commonly easy the computation of these kind of indices, but they could be unable to capture non-stationary patterns.

An alternative methodology that has been proposed to study travelling and standing waves is complex Empirical Orthogonal Functions (Horel 1984). This method extends EOF analysis to capture oscillations with varying amplitude and phase and has been applied to the time domain. For instance, Krokhnin and Luxemburg (2007) applied cEOF to station-based monthly precipitation anomalies and monthly temperature anomalies in the Eastern Siberia and the Far East region to characterise the main modes of variability and their connection to teleconnection indices. Similarly, Gelbrecht, Boers, and Jürgen Kurths (2018) used cEOF applied to daily precipitation from reanalysis to study the propagating characteristics of the South American Monsoon. To our knowledge, complex EOF has not been applied in the spatial domain to capture the phase-varying nature of planetary waves.

Some of the zonally asymmetric patterns of the SH circulation variability described previously, appear to have experienced secular changes. For instance, M. Raphael (2003) found that the amplitude of the zonal wave 1 experienced a large increase and that the zonal wave 3 experienced changes in its annual cycle between 1958 and 1996. However, little is known yet about variability and trends of these patterns.

The general goal of this study is to improve the description and understanding of the zonally asymmetric extratropical SH circulation using complex Empirical Orthogonal Functions, which allow to describe phase varying planetary waves with variable amplitudes along a latitude circle. In addition,

it is proposed to expand the knowledge of the simultaneous behaviour of SH asymmetric circulation in the troposphere and the stratosphere.

We restrict this paper to the September-October-November (SON) trimester. We chose this season because it showed the strongest and more clearly interpretable results in a preliminary analysis of the four seasons. This is consistent with previous research that shows that this season experiences a maximum in tropical teleconnections (Cazes-Boezio, Robertson, and Mechoso 2003) and stratosphere-troposphere interactions (Lim, Hendon, and Thompson 2018).

In Section 2 we describe the methods. In Section 3.1 we analyse the spatial patterns of each complex EOF. In Section 3.2 we study the spatial regressions with geopotential height and temperature anomalies. In Section 3.3 we analyse the relationship between cEOF1 and Ozone, and between cEOF2 with the SAM and the PSA. In Section 3.4 we study tropical forcings that explain the variability of each cEOF. Finally, in Section 3.5 we show the relationship between these modes of variability and precipitation anomalies in South America and Oceania.

## 2 Data and Methods

methods

### 2.1 Data

data

We used monthly geopotential height, air temperature, ozone mixing ratio, and total ozone column (TOC) at  $2.5^\circ$  longitude by  $2.5^\circ$  latitude of horizontal resolution and 37 vertical isobaric levels from the European Centre for Medium-Range Weather Forecasts Reanalysis version 5 [ERA; Hersbach et al. (2019)] for the period 1979 – 2019. Most of our analysis is restricted to the post-satellite era to avoid any confounding factors arising from the incorporation of satellite observations, but we also used the preliminary back extension of ERA5 from 1950 to 1978 (Bell et al. 2020) to describe long-term trends. We derived streamfunction at 200 hPa from ERA5 vorticity using the FORTRAN subroutine FISHPACK (Adams, Swartztrauber, and Sweet 1999) and we computed horizontal wave activity fluxes following Plumb (1985). Sea Surface Temperature (SST) monthly fields are from Extended Reconstructed Sea Surface Temperature (ERSST) v5 (Huang et al. 2017) and precipitation monthly data from the CPC Merged Analysis of Precipitation (P. Xie and Arkin 1997), with a  $2.5^\circ$  resolution in latitude and longitude. The rainfall gridded dataset is based on information from different sources such as rain gauge observations, satellite inferred estimations and the NCEP-NCAR reanalysis, and it is available since 1979 to present.

The Oceanic Niño Index (ONI, Bamston, Chelliah, and Goldenberg 1997) comes from NOAA’s Climate Prediction Center and the Dipole Mode Index (DMI, Saji and Yamagata 2003) from Global Climate Observing System Working Group on Surface Pressure.

## 2.2 Methods

methods-1

The study is restricted to the spring season, defined as the September-October-November (SON) trimester. We compute seasonal means for the different variables, averaging monthly values weighted by the number of days in each month. We use the 200 hPa level to represent the high troposphere and 50 hPa to represent the lower stratosphere.

The amplitude of the zonal waves was obtained through the Fourier transform of the spatial field at each latitude circle. For the analysis of wave 1, we computed its amplitude and phase by averaging (area-weighted) the data for each variable and each SON between 75°S and 45°S, and then extracting the wave-1 component of the Fourier spectrum. We chose this latitude band because it is wide enough to capture most of the relevant anomalies of SH mid-latitudes.

We computed the level-dependent SAM index as the leading EOF of year-round monthly geopotential height anomalies south of 20°S at each level for the whole period (Baldwin and Thompson 2009). We further split the SAM into its zonally symmetric and zonally asymmetric components (S-SAM and A-SAM indices respectively). These indices were obtained by projecting the zonally asymmetric and zonally symmetric part of the SAM spatial pattern onto monthly geopotential height fields, as proposed by Campitelli, Díaz, and Vera (2022). Seasonal indices of the Pacific South American patterns (PSA1 and PSA2) were calculated, in agreement with Mo and Paegle (2001), as the third and fourth leading EOF of seasonal mean anomalies for 500-hPa geopotential heights at SH.

Linear trends were computed by Ordinary Least Squares (OLS) and the 95% confidence interval was computed assuming a t-distribution with the appropriate residual degrees of freedom (D. Wilks 2011).

## 2.3 Complex Empirical Orthogonal Functions (cEOF)

complex-empirical-orthogonal-functions-ceof

In the standard EOF analysis, zonal waves may appear as pairs of (possibly degenerated) EOFs representing similar patterns but shifted in phase (Horel 1984). Figure 1 shows the four leading EOFs of SON geopotential height zonal anomalies at 50 hPa south of 20°S. It is clear that the first two EOFs represent a single phase-varying zonal wave 1 pattern and the last two represent a similarly phase-varying pattern with shorter wavenumber and four centres of action shifted by 1/4 wavelength. A similar EOF structure can be seen in 200 hPa (not shown). Since each pair of EOFs seems to represent the same phase-varying structure, it would be desirable to combine them into a single pattern described by amplitude and phase.

Complex Empirical Orthogonal Functions (cEOF) are a useful method for characterising zonal waves, associated with phase-varying structures (Horel 1984). This method involves computing EOF on the analytic representation of the original field. That representation is a complex field in which the real part

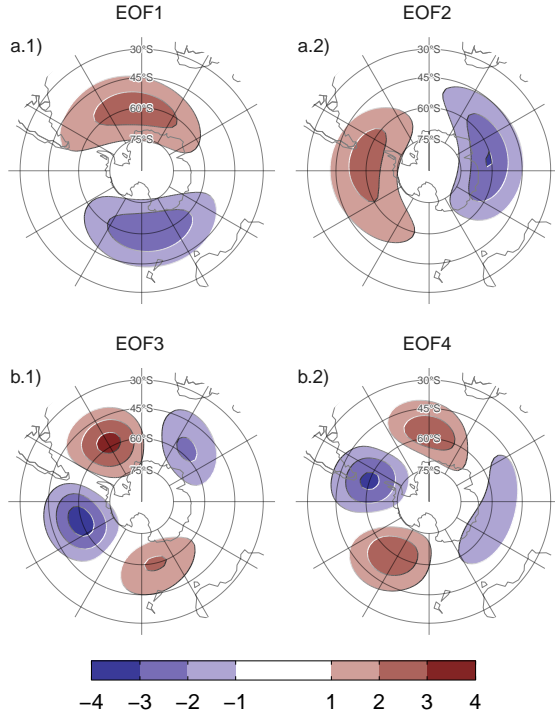


Fig. 1: Spatial patterns of the four leading EOFs of SON zonal anomalies of geopotential height at 50 hPa south of 20°S for the 1979 – 2019 period (arbitrary units).

is the original data and the imaginary part is the original data shifted by  $90^\circ$  at each spectral frequency – i.e. its Hilbert transform. The Hilbert transform is usually understood in terms of time-varying signal. However, in this work we apply the Hilbert transform at each latitude circle and at each considered time. Since each latitude circle is a periodic domain, this procedure does not suffer from edge effects.

The result of the cEOF methodology is a set of complex spatial patterns and complex time series. The real and imaginary part of each spatial pattern represent the two phases of wave-like spatial patterns that are in quadrature. The magnitude and argument of each complex time series represent the amplitude and phase of each zonal wave.

The cEOF methodology is applied to SON geopotential height zonal anomalies south of  $20^\circ\text{S}$  separately at 50 and 200 hPa. Table 1 shows the coefficient of determination between time series of the amplitude of each cEOF across levels. There is a high degree of correlation between the magnitude of the respective cEOF1 and cEOF2 at each level. The spatial patterns of the 50 hPa and 200 hPa cEOFs are also similar (not shown).

Table 1: <sup>tab:corr-ceof-split</sup>Coefficient of determination ( $R^2$ ) between the absolute magnitude of complex EOFs computed separately at 200 hPa and 50 hPa (p-values lower than 0.01 in bold).

200 hPa	50 hPa		
	cEOF1	cEOF2	cEOF3
cEOF1	<b>0.29</b>	0.01	0.03
cEOF2	0.00	<b>0.59</b>	0.02
cEOF3	0.00	0.00	0.01

Both the spatial pattern similarity and the high temporal correlation of cEOFs computed at 50 hPa and 200 hPa suggest that these are, to a large extent, modes of joint variability. This motivates the decision of performing complex EOF jointly between levels. Therefore cEOFs were computed using data from both levels at the same time. In that sense each cEOF has a spatial component that depends on longitude, latitude and level, and a temporal component that depends only on time.

The phase of cEOFs is defined up to an additive constant. For real EOFs, this constant can be either 0 or  $\pi$ , corresponding to a change in sign. For cEOFs, it can be any real number between 0 and  $2\pi$  (Horel 1984), corresponding to rotations in the complex plane. Since any choice is arbitrary and equally valid, we chose the phase of each cEOF so that the real or imaginary parts are aligned with meaningful phases in our analysis.

Preliminary analysis showed that the first cEOF was closely related to the the zonal wave 1 of Total Ozone Column and the second cEOF was closely related to ENSO. Therefore, to aid in the interpretation, we chose the phases of each cEOF so that these relationships are aligned with one of the complex components.

We chose the phase of cEOF1 so that the time series corresponding to the real part has the maximum correlation with the zonal wave 1 of Total Ozone Column between 75°S and 45°S. And we chose the phase of cEOF2 so that the coefficient of determination between the Oceanic Niño Index (Bamston, Chelliah, and Goldenberg 1997) and the real part is minimized, which also nearly maximizes the correlation with the imaginary part.

This procedure does not create spurious correlations, it only takes an existing relationship and aligns it with a specific phase.

While we compute these complex principal components using data from 1979 to 2019, we extended the complex time series back to the 1950 – 1978 period by projecting monthly geopotential height zonal anomalies standardised by level south of 20°S onto the corresponding spatial patterns.

We performed linear regressions to quantify the association between the cEOFs and other variables (e.g. geopotential height, temperature, precipitation, and others). For each cEOF, we computed regression maps by fitting a multiple linear model involving both the real and the imaginary part. To

obtain the linear coefficients of a variable  $X$  with the imaginary and real parts of each cEOF we fit the equation

$$X(\lambda, \phi, t) = \alpha(\lambda, \phi) \text{Im}(\text{cEOF}) + \beta(\lambda, \phi) \text{Re}(\text{cEOF}) + X_0(\lambda, \phi) + \epsilon(\lambda, \phi, t)$$

where  $\lambda$  and  $\phi$  are the longitude and latitude,  $t$  is the time,  $\alpha$  and  $\beta$  are the linear regression coefficients for imaginary and real parts respectively,  $X_0$  and  $\epsilon$  are the constant and error terms respectively.

We evaluated statistical significance using a two-sided t-test and, in the case of regression maps, p-values were adjusted by controlling for the False Discovery Rate (Benjamini and Hochberg 1995; D. S. Wilks 2016) to avoid misleading results from the high number of regressions (Walker 1914; Katz and Brown 1991).

## 2.4 Computation procedures

### computation-procedures

We performed all analysis in this paper using the R programming language (R Core Team 2020), using data.table (Dowle and Srinivasan 2020) and metR (Campitelli 2020) packages. All graphics are made using ggplot2 (Wickham 2009). We downloaded data from reanalysis using the ecmwfr package (Hufkens 2020) and indices of ENSO and Indian Ocean Dipole with the rsoi package (Albers and Campitelli 2020). The paper was rendered using knitr and rmarkdown (Y. Xie 2015; Allaire et al. 2020).

## 3 Results

### results

### 3.1 cEOF spatial patterns

#### spatial

To describe the variability of the circulation zonal anomalies, the spatial and temporal parts of the first two leading cEOFs of zonal anomalies of geopotential height at 50 hPa and 200 hPa, computed jointly at both levels, are shown in Figures 2 and 3. The first mode (cEOF1) explains 82% of the variance of the zonally anomalous fields, while the second mode (cEOF2) explains a smaller fraction (7%). In the spatial patterns (Fig. 2), the real and the imaginary components are in quadrature by construction, so that each cEOF describe a single wave-like pattern whose amplitude and position (i.e. phase) is controlled by the magnitude and phase of the temporal cEOF. The wave patterns described by these cEOFs match the patterns seen in the traditional EOFs of Figure 1.

The cEOF1 (Fig. 2 column a) is a hemispheric wave 1 pattern with maximum amplitude at high latitudes. At 50 hPa the Real cEOF1 has the maximum of the wave 1 at 150°E and at 200 hPa, the maximum is located at around 175°E indicating a westerly shift in phase. The cEOF2 (Fig. 1 column b) shows also a zonal wave-like structure with maximum amplitude at high latitudes, but with shorter spatial scales. In particular, the dominant structure at both



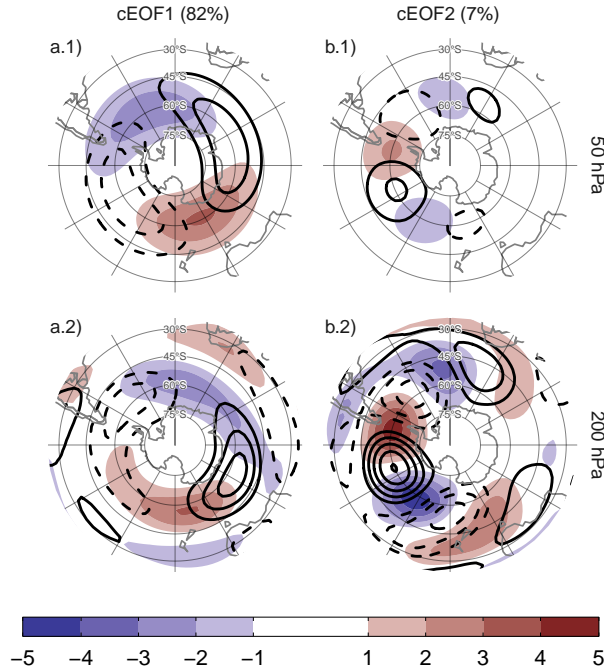


fig:ceofs-1  
 Fig. 2: Spatial patterns for the two leading cEOFs of SON zonal anomalies of geopotential height at 50 hPa and 200 hPa for the 1979 – 2019 period. The shading (contours) corresponds to real (imaginary) part. Arbitrary units.

levels is a wave 3 but with larger amplitude in the pacific sector. This modulated amplitude more evident at 200 hPa. There is no apparent phase shift with height but the amplitude of the pattern is greatly reduced in the stratosphere, suggesting that this barotropic mode represents mainly tropospheric variability.

There is no significant simultaneous correlation between cEOFs time series. Both cEOFs show year-to-year variability but show no evidence of decadal variability (Fig. 3). Because the geopotential fields that enter into the cEOFs algorithm are anomalies with respect to the zonal mean instead of the time mean, the cEOFs have non zero temporal mean. However, cEOF2's mean is almost zero, which indicates that only cEOF1 includes variability that significantly projects onto the mean zonally anomalous field.

A significant upward trend in the real component of cEOF1 is evident (Fig. 3a.1,  $p$ -value = 0.0037) while there is no significant trend in any of the complex components of cEOF2. The positive trend in the Real cEOF1 translates into a positive trend in cEOF1 magnitude, but not systematic change in phase (not shown). This long-term change indicates an increase in the magnitude of the high latitude zonal wave 1. In agreement, M. Raphael (2003) detected a step change after around 1975 in the temporal evolution of leading

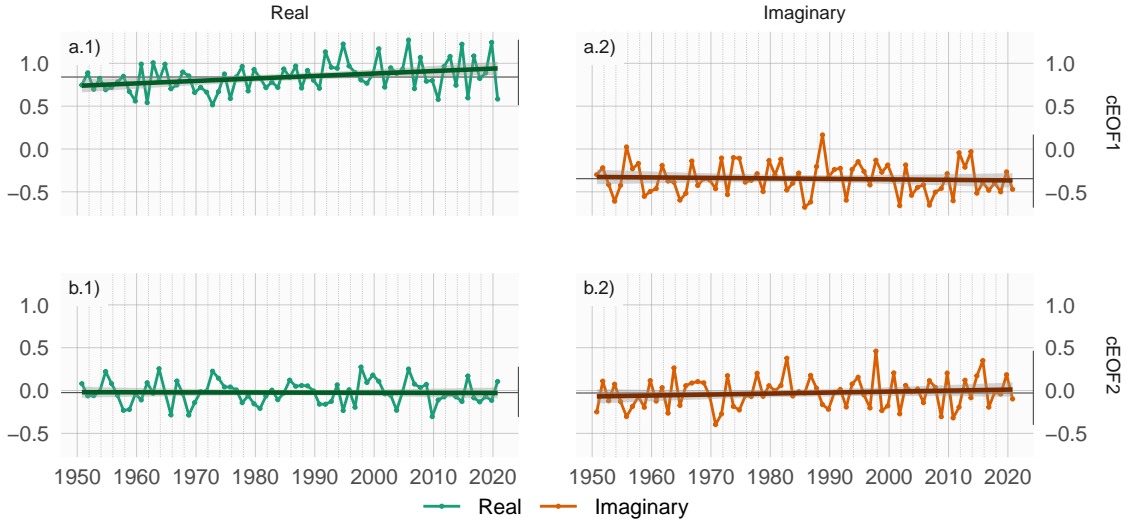


Fig. 3: Time series of the two leading cEOFs of SON zonal anomalies of geopotential height at 50 hPa and 200 hPa. cEOF1 (row a) and cEOF2 (row b) separated in their real (column 1) and imaginary (column 2) components. Dark straight line is the linear trend. Black horizontal and vertical line mark the mean value and range of each time series, respectively. `fig:extended-series`

290 EOF computed from August-September-October 500 hPa zonal geopotential  
 291 height anomalies, which is similar to the cEOF1.

### 292 3.2 cEOFs Regression maps

#### regressions

293 In the previous section, cEOFs were applied to zonal anomalies, that is anom-  
 294 alies derived by removing the zonally mean values in order to isolate the main  
 295 characteristics of the main zonal waves characterizing the circulation in the  
 296 SH. In this section, regression fields were computed using the full fields of  
 297 the variables in order to describe the influence of the cEOFs on the temporal  
 298 anomalies.

299 Figure 4 shows regression maps of SON geopotential height anomalies upon  
 300 cEOF1. At 50 hPa (Figure 4 row a), the Real cEOF1 is associated with a  
 301 monopole centred over the Ross Sea. The Imaginary cEOF1 is associated with  
 302 a clear wave 1 pattern with maximum over the coast of East Antarctica.

303 At 200 hPa (Figure 4 row b) the Real cEOF1 shows a single area of pos-  
 304 itive anomalies spanning West Antarctica surrounded by opposite anomalies  
 305 in lower latitudes with its centre shifted slightly eastward compared with the  
 306 upper level anomalies. The Imaginary cEOF2. The Imaginary cEOF1 shows a  
 307 much more zonally symmetrical pattern resembling the negative SAM phase

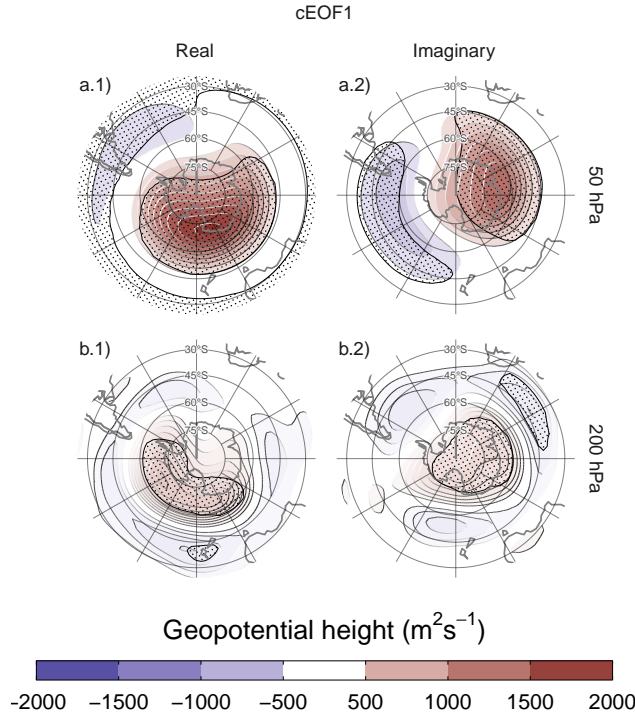


fig:eof1-regr-gh  
 Fig. 4: Regression of SON geopotential height anomalies ( $m^2s^{-1}$ ) with the (column 1) real and (column 2) imaginary parts of the first cEOF for the 1979 – 2019 period at (row a) 50 hPa and (row b) 200 hPa. These coefficients come from multiple linear regression involving the real and imaginary parts. Areas marked with dots have p-values smaller than 0.01 adjusted for False Detection Rate.

(Fogt and Marshall 2020). Both components of cEOF1 could be associated to zonal anomalies in the upper troposphere jet stream intensity.

Therefore, the magnitude and phase of the cEOF1 are associated with the magnitude and phase of a zonal wave only in the stratosphere. While in the troposphere, they are associated with slightly off-centre monopoles.

Figure 5 shows the regression maps of geopotential height anomalies upon the cEOF2. Wave trains similar to those identified for cEOF2 patterns (Fig 2) can be distinguished. Regressed anomalies associated with the Real cEOF2 are  $90^\circ$  out of phase with those associated with the Imaginary cEOF2. All fields have a dominant zonal wave 3 limited to the western hemisphere, over the Pacific and Atlantic Oceans. cEOF2 then represents an equivalent barotropic wave train that is very similar to the the PSA Patterns (Mo and Paegle 2001). Comparing the location of the positive anomaly near  $90^\circ W$  in column b of Figure 5 with Figures 1.a and b from Mo and Paegle (2001), the Real cEOF2

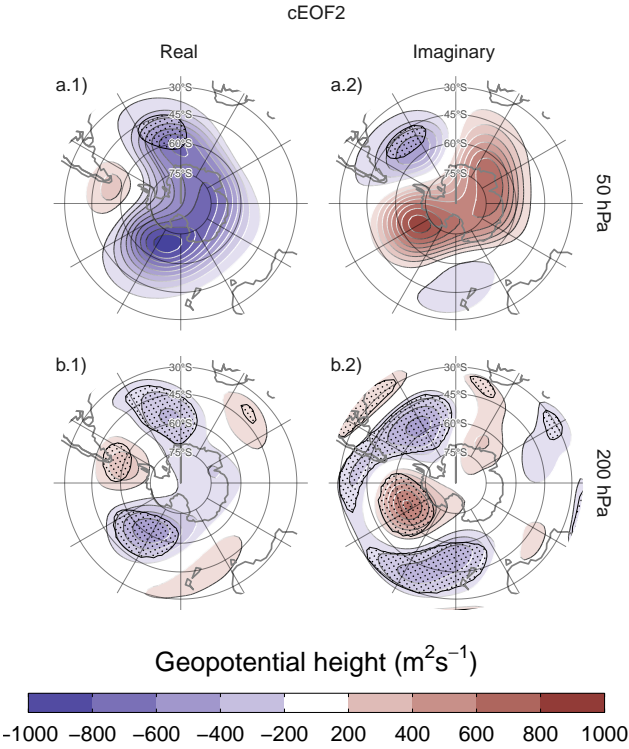


Fig. 5: Same as Figure 4 but for cEOF2.

Table 2: Correlation coefficients ( $r$ ) between cEOF2 components and the PSA1 and PSA2 modes computed as Mo and Paegle (2001) for the 1979 – 2019 period. 95% confidence intervals in parenthesis. p-values lower than 0.01 in bold.

PC	cEOF2	
	Real	Imaginary
PSA1	0.26 (CI: -0.04 – 0.52)	<b>0.82 (CI: 0.69 – 0.9)</b>
PSA2	<b>0.79 (CI: 0.63 – 0.88)</b>	-0.02 (CI: -0.32 – 0.29)

regression map could be identified with PSA2, while the Imaginary cEOF2 resembles PSA1.

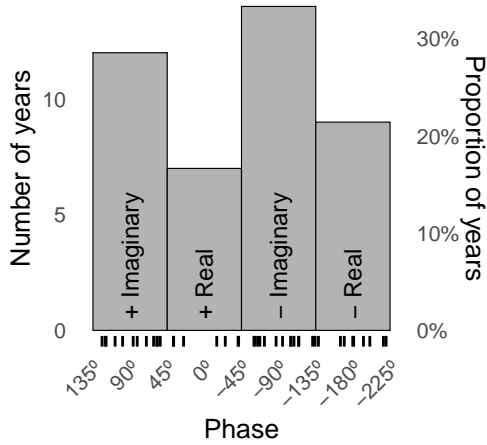


fig:phase-histogram  
 Fig. 6: Histogram of phase distribution of cEOF2 phase for the 1979 – 2019 period. Bins are centred at  $90^\circ$ ,  $0^\circ$ ,  $-90^\circ$ ,  $-180^\circ$  with a binwidth of  $90^\circ$ . The small vertical lines near the horizontal axis mark the observations.

### 3.3 cEOFs relationship with known modes of variability

other-variables

#### 3.3.1 PSA

psa

Given the similarity between the cEOF2 regression maps (Fig. 5) and documented PSAs we study the relationship between these modes. Table 2 shows the correlations between the two PSA indices and the time series for Real and Imaginary phases of cEOF2. As anticipated by Figure 5, there is a strong positive correlation between PSA1 and Imaginary cEOF2, and also between PSA2 and Real cEOF2. On the other hand, there is no significant relationship between PSA1 and Real cEOF2, and between PSA2 and Imaginary cEOF2. As a result, cEOF2 represents well both the spatial structure and temporal evolution of the PSA modes, so it is possible to make an association between its two phases and the two PSA modes. The same phase election for cEOF2 that maximises the relationship between ENSO and Imaginary cEOF2, also maximises the association between cEOF2 components and PSA modes.

Figure 6 shows an histogram that counts the number of SON seasons in which the cEOF2 phase was close to each of the four particular phases (positive/negative of real/imaginary component), with the observations for each season marked as rugs on the horizontal axis. In 62% of seasons cEOF2 has a phase similar to either the negative or positive imaginary phase, making the imaginary phase the most common phase. This is also, by construction, the phase that is most correlated with ENSO. Therefore, the Imaginary cEOF2 explains more variance than the Real cEOF2 and conventional EOF analysis will tend to separate the two.

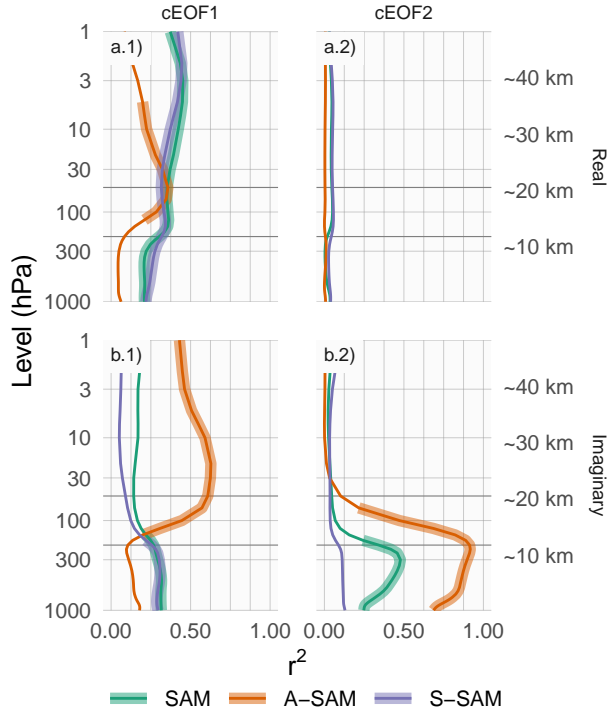


Fig. 7: Coefficient of determination ( $r^2$ ) between each component of cEOFs and the SAM, Asymmetric SAM (A-SAM) and Symmetric SAM (S-SAM) indices computed at each level for the 1979 – 2019 period. Thick lines represent estimates with  $p$ -value  $< 0.01$  corrected for False Detection Rate (Benjamini and Hochberg 1995).

This phase preferences is in agreement with Irving and Simmonds (2016), who found a bimodal distribution to PSA-like variability (compare our Figure 6 with their Figure 6).

### 3.3.2 SAM

We now explore the relationship between SAM and the cEOFs motivated by the resemblance between cEOFs regression maps and SAM patterns shown in the previous section. To that end, we computed the coefficient of determination between the cEOFs time series and the three SAM indices (SAM, A-SAM and S-SAM) defined by Campitelli, Díaz, and Vera (2022) at each vertical level (Fig. 7). The SAM index is statistically significant correlated with the Real cEOF1 in all levels, and with the Imaginary cEOF1 and Imaginary cEOF2 in the troposphere. On the other hand, correlations between SAM and the Real cEOF2 are non-significant.

The relationship between the SAM and cEOF1 in the troposphere is explained entirely by the zonally symmetric component of the SAM as shown by the high correlation with the S-SAM below 100 hPa and the low and statistically non-significant correlations between the A-SAM and either the Real or Imaginary cEOF1. In the stratosphere, the Real cEOF1 is correlated with both A-SAM and S-SAM, while the Imaginary cEOF1 is highly correlated only with the A-SAM. These correlations are consistent with the regression maps of geopotential height in Figure 4 and their comparison with those obtained for SAM, A-SAM and S-SAM by Campitelli, Díaz, and Vera (2022).

In the case of Imaginary cEOF2, the correlation between SAM and Imaginary cEOF2 for the troposphere is associated to the asymmetric variability of the SAM. Indeed, the Imaginary cEOF2 shares up to 92% variance with the A-SAM and only 12% at most with the S-SAM (Figure 7.b2). Such extremely high correlation between A-SAM and Imaginary cEOF2 suggests that the methodology proposed in this work is able to characterise the zonally asymmetric component of the SAM described previously by Campitelli, Díaz, and Vera (2022).

### 3.3.3 Temperature and Ozone

#### temperature-and-ozone

The influence of cEOFs variability on air temperature was also evaluated. Figure 8 shows regression maps of air temperature anomalies at 50 hPa and 200 hPa upon cEOF1. In both levels, the Real cEOF1 is associated with a positive monopole over the South Pole with its centre moved slightly towards 150°E (Fig. 8 column 1). On the other hand, the regression maps on the Imaginary cEOF1 show a more clear wave 1 pattern with its maximum around 60°E. The distribution of temperature regression coefficients at 50 hPa and at 200 hPa mirror the geopotential height regression maps at 50 hPa (Fig. 4).

Figure 9 shows the vertical distribution of the regression coefficients on cEOF1 from zonal anomalies averaged between 75°S and 45°S of air temperature and of ozone mixing ratio. Temperature zonal anomalies associated with cEOF1 show a clear wave 1 pattern for both real and imaginary components throughout the atmosphere above 250 hPa with a sign reversal above 10 hPa. As a result of the hydrostatic balance, this is the level in which the geopotential anomaly have maximum amplitude (not shown).

The maximum ozone regressed anomalies match with the minimum temperature anomalies above 10 hPa and with the maximum temperature anomalies below 10 hPa (Fig. 9). Therefore, the ozone zonal wave 1 is anticorrelated with the temperature zonal wave 1 in the upper stratosphere, and directly correlated in the upper stratosphere. This change in phase is observed in ozone anomalies forced by planetary waves that reach the stratosphere (Hartmann and Garcia 1979; Wirth 1993; Smith 1995). In the photochemically-dominated upper stratosphere, cold temperatures inhibit the destruction of ozone, explaining the opposite behaviour for both variables. On the other hand, in the advectively-dominated lower stratosphere, ozone anomalies are 90° out of phase with horizontal and vertical transport, which are in addition 90° out of

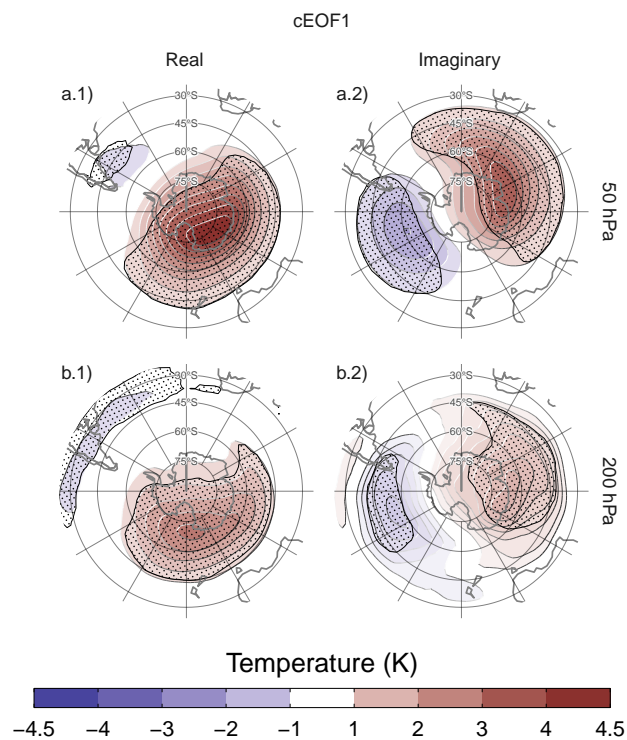


Fig. 8: Same as Figure 4 but for air temperature (K).

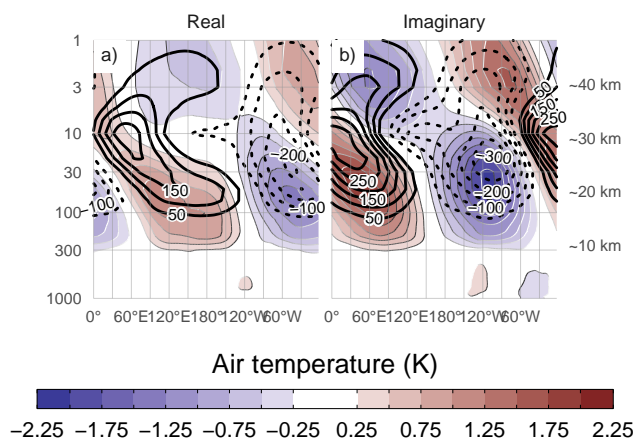


Fig. 9: Regression of SON zonal anomalies averaged between 75°S and 45°S of mean air temperature (shaded, Kelvin) and ozone mixing ratio (contours, negative contours with dashed lines, labels in parts per billion by mass) with the (a) Real and (b) Imaginary components of the cEOF1 for the 1979 – 2019 period.



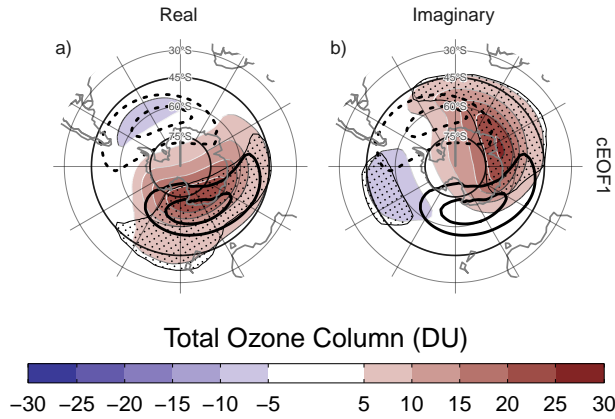


Fig. 10: Regression of SON mean Total Ozone Column anomalies (shaded, Dobson Units) with the (a) real and (b) imaginary components of the cEOF1 for the 1979 – 2019 period. On contours, the mean zonal anomaly of Total Ozone Column (negative contours in dashed lines, Dobson Units). Areas marked with dots have p-values smaller than 0.01 adjusted for False Detection Rate.

phase with temperature anomalies, resulting in same sign anomalies for the response of both variables

The regression maps of TOC anomalies upon cEOF1 (Fig. 10) show zonal wave 1 patterns associated with both components of cEOF1. The climatological position of the springtime Ozone minimum (ozone hole) is outside the South Pole and towards the Weddell Sea (e.g. Grytsai 2011). Thus, the Real cEOF1 regression field (Figure 10a) coincides with the climatological position of the ozone hole, while it is 90° out of phase for the Imaginary cEOF1. The temporal correlation between the amplitudes of TOC planetary wave 1 and cEOF1 is 0.79 (CI: 0.63 – 0.88), while the correlation between their phases is -0.85 (CI: -0.92 – -0.74). Consequently, cEOF1 is strongly related with the SH ozone variability.

### 3.4 Tropical sources

The connections between cEOFs and Tropical sources are also assessed, to explore plausible forcings for the described cEOFs patterns. Figure 11 shows the regression maps of Sea Surface Temperatures (SST) and streamfunction anomalies at 200 hPa respectively upon standardised cEOF2,. Besides showing the regression maps for the Real and Imaginary components, we including the corresponding regressions for two intermediate directions (corresponding to 45° and 135°).

The Imaginary cEOF2 (second row) is associated with strong positive SST anomalies on the Central Pacific and negative anomalies over an area across

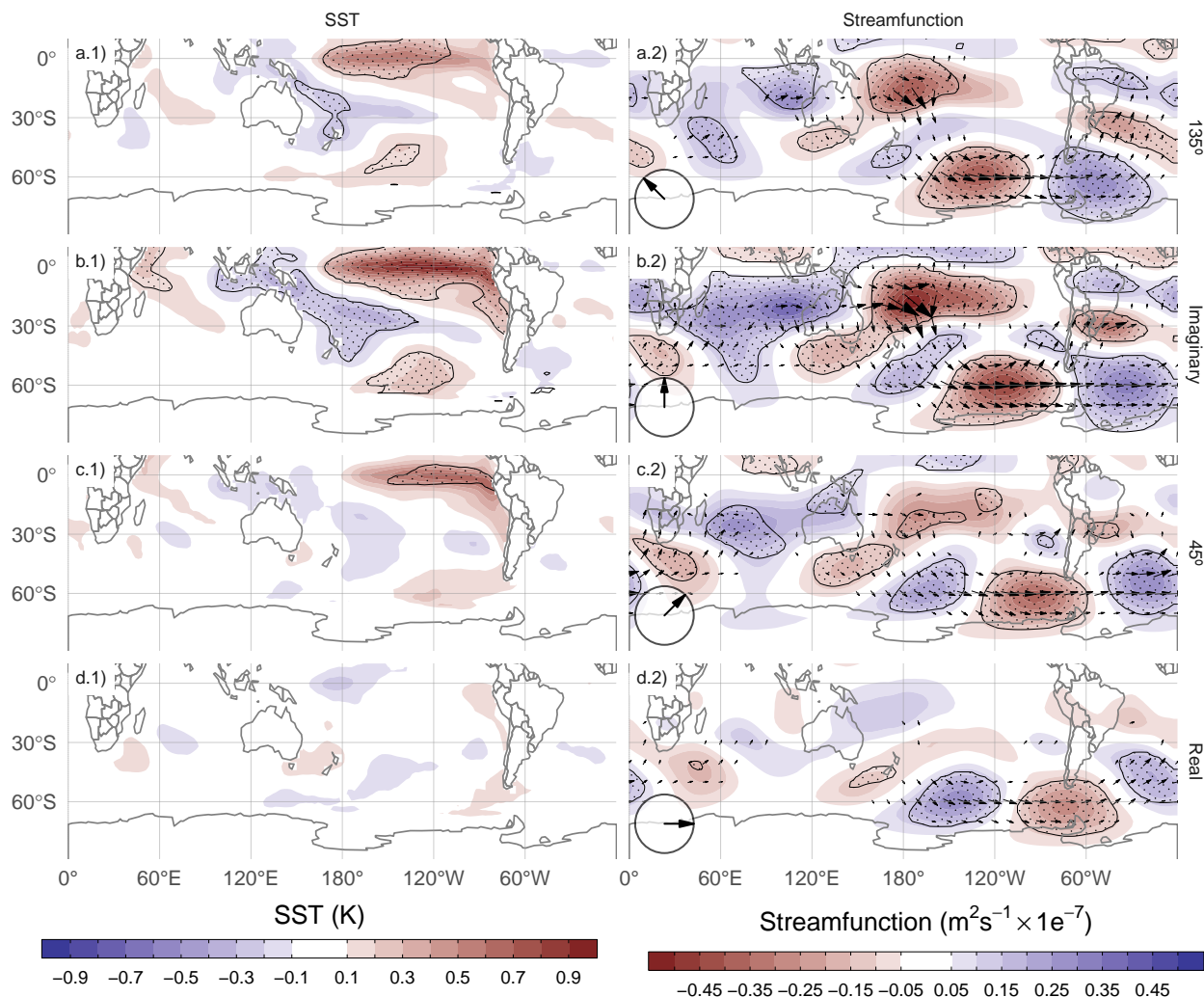


Fig. 11: Regression of SST (K, left column ) and streamfunction zonal anomalies ( $m^2/s \times 10^{-7}$ , shaded) with their corresponding activity wave flux (vectors) (right column) upon cEOF2 different phases (illustrated in the lower-left arrow) for the 1979 – 2019 period. Areas marked with dots have p-values smaller than 0.01 adjusted for FDR.

fig:sst-psi-2

northern Australia, New Zealand the South Pacific Convergence Zone (SPCZ) (Figure 11.b1). The regression field of SST anomalies bears a strong resemblance with canonically positive ENSO (Bamston, Chelliah, and Goldenberg 1997). Indeed, there is a significant and very high correlation (0.76 (CI: 0.6 – 0.87)) between the ONI and the Imaginary cEOF2 time series. Besides the Pacific ENSO-like pattern, there are positive anomalies in the western Indian

Ocean and negative values in the eastern Indian Ocean, resembling a positive Indian Ocean Dipole (Saji et al. 1999). Unsurprisingly, the correlation between the Imaginary cEOF2 and the DMI is 0.62 (CI: 0.38 – 0.78).

The Imaginary cEOF2 is associated with strong wave-like streamfunction anomalies emanating from the tropics (Figure 11.b2), both from the Central Pacific sector and the Indian Ocean. These atmospheric response is consistent with the effect of ENSO and the Indian Ocean Dipole on the extratropics: the SST anomalies initiate anomalous tropical convection that excites Rossby waves that propagate meridionally towards higher latitudes (Mo 2000; Cai et al. 2011; Nuncio and Yuan 2015).

The cEOF2 is not associated with the same tropical SSTs for all their phases. Figure 11.d1 and d2 show that the Real cEOF2 is not associated either with any significant SST nor streamfunction anomalies in the tropics. As a result, the correlation between the Real cEOF2 and ENSO is also not significant (0 (CI: -0.3 – 0.3)). Meanwhile, Rows a and c in Fig. 11 show that the intermediate phases are still associated with significant SST anomalies over the Pacific Ocean, but with slightly different location. The 135° phase is associated with SST in the central Pacific (Fig. 11a.1), while the 45° phase is associated with SST in the eastern Pacific (Fig. 11c.1), which correspond roughly to the Central Pacific and Eastern Pacific and “flavours” of ENSO, respectively (Kao and Yu 2009). Both of these phases could be also associated to wave trains generated in the region surrounding Australia and propagates toward the extra-tropics.

To better explore the relationship between tropical forcing and phases of the cEOF2, Figure 12 shows the ONI index plotted against the cEOF2 phase for each SON trimester between 1979 and 2019, highlighting years in which the magnitude of cEOF2 is above the median. In years with positive (negative) ONI, the cEOF2 phase is mostly around 90° (-90°), corresponding with positive (negative) Imaginary component. In the neutral ENSO seasons, the cEOF2 phase is much more variable. The black line in Figure 12 is a sinusoidal fit of the relationship between ONI and cEOF2 phase. The  $r^2$  corresponding to the fit is 0.57, statistically significant with p-value < 0.001, indicating a quasi-sinusoidal relation between these two variables.

The correlation between the absolute magnitude of the ONI index and the cEOF2 amplitude is 0.45 (CI: 0.17 – 0.66). However, this relationship is mostly driven by the three years with strongest ENSO events in the period (2015, 1997, and 1982) which coincide with the three years with strongest cEOF2 magnitude (not shown). If those years are removed, the correlation becomes non-significant (0.04 (CI: -0.28 – 0.35)). Furthermore, even when using all years, the Spearman correlation –which is robust to outliers– is also non-significant (0.2, p-value= 0.21). Therefore, although the location of tropical SST seem to have an effect in defining the phase of the cEOF2, the relationship between the magnitude of cEOF2 and ONI remains uncertain.

It could be concluded that the wave train represented by cEOF2 can be both part of the internal variability of the extratropical atmosphere or forced by tropical SSTs. In the former case, the wave train has little phase preference.

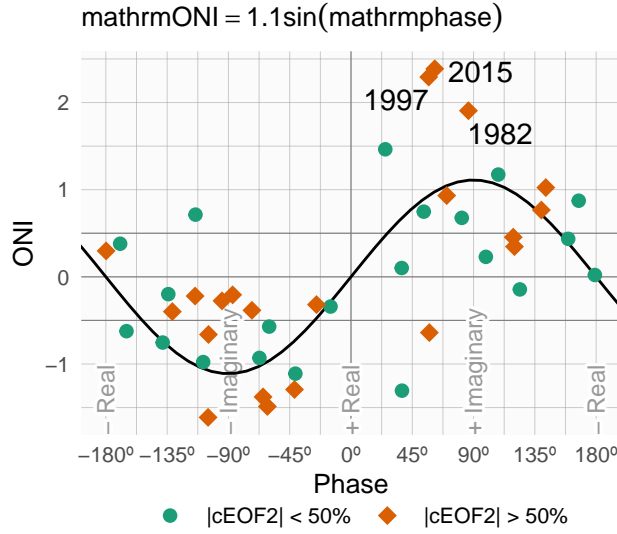


Fig. 12: SON ONI values plotted against cEOF2 phase for the 1979 – 2019 period. Years with magnitude of cEOF2 greater (smaller) than the 50th percentile are shown as orange diamonds (green circles). Black line is the fit  $\text{ONI} \sim \sin(\text{phase})$  computed by weighted OLS using the magnitude of the cEOF2 as weights.

However, when cEOF2 is excited by tropical SST variability, it tends to remain locked to the imaginary phase. This explains the relative over-abundance of years with cEOF2 near positive and negative imaginary phase in Figure 6.

Unlike the cEOF2 case, there are no significant SST regressed anomalies associated with either the Real or Imaginary cEOF1 (Sup. Figure A.1). Consistently, streamfunction anomalies do not show any tropical influence. Instead, the real and Imaginary cEOF1 are associated with zonally wave activity fluxes in the extra-tropics around 60°S, except for an equatorward flow from the coast of Antarctica around 150°E in the Real component. This suggests that the variability of cEOF1 is driven primary by the internal variability of the extra-tropics.

### 3.5 Precipitation and 2-metre temperature

#### precipitation

Figure 8 shows the variance of the 2-meter temperature or precipitation anomalies explained variance by the multiple linear model of Real cEOF1 and Imaginary cEOF1 (column 1), and Real cEOF2 and Imaginary cEOF2 (column 2). The variance explained by cEOF1 for precipitation anomalies is extremely low and also for most of the temperature anomalies, except for the eastern western of Antarctica (Fig. 8a.1).

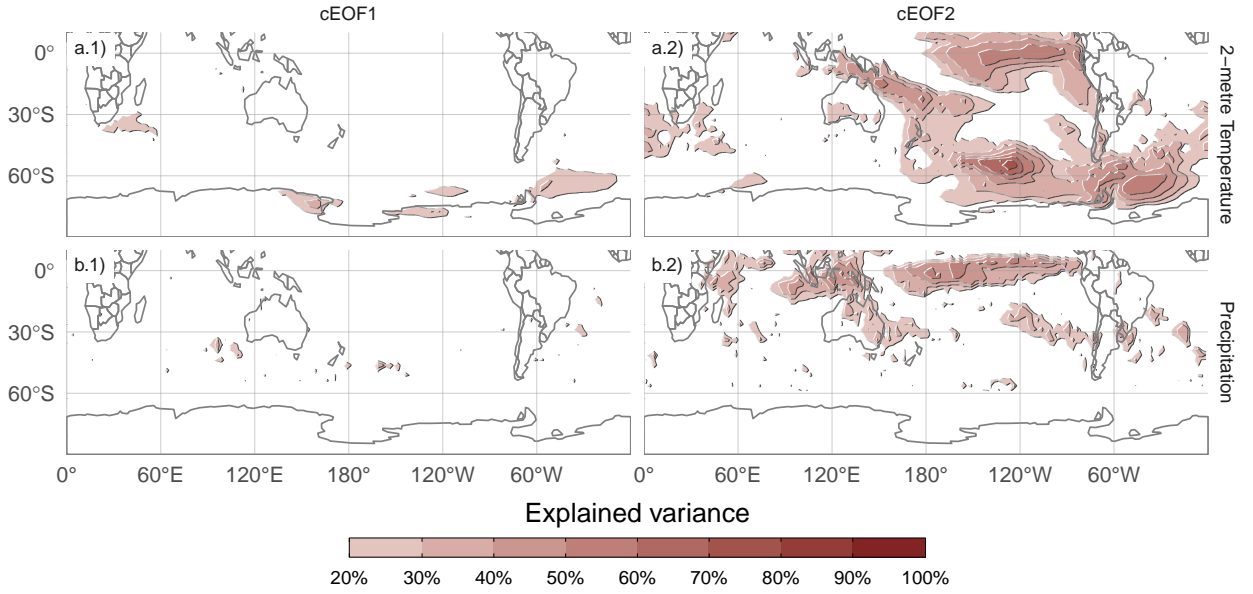


Fig. 13: Explained variance ( $r^2$  as percentage) of 2-metre temperature (row a) and precipitation (row b) anomalies by the regression upon cEOF1 (column 1) and cEOF2 (column 2).

On the other hand, the cEOF2 explained variance is greater than 50% in some regions for both variables (Fig. 8 column 2). For 2-metre temperature, there are high values in the tropical Pacific and the SPCZ, as well as the region following an arc between New Zealand and the South Atlantic, with higher values in the Southern Ocean. Over the continents, there are moderate values of about 30% variance explained in southern Australia, Southern South America and the Antarctic Peninsula. For precipitation, there are high values over the tropics. At higher latitudes, moderate values are observed over eastern Australia and some regions of southern South America.

Since the cEOF1 has a relatively weak signal in the surface variables explored here, we will only focus on the cEOF2 influence.

Figure 14 shows regression maps of 2-metre temperature (column 1) and precipitation (column 2) anomalies upon different phases of standardised cEOF2.

Temperature anomalies associated with the Imaginary cEOF (Fig. 14.b1) show positive values in the tropical Pacific, consistent with SSTs anomalies associated with the same phase (Fig. 11.b1).

At higher latitudes there is a wave-like pattern of positive and negative values that coincide with the nodes of the 850 hPa geopotential height regression patterns. This is consistent with temperature anomalies produced by meridional advection of temperature by the meridional winds arising from geostrophic balance.

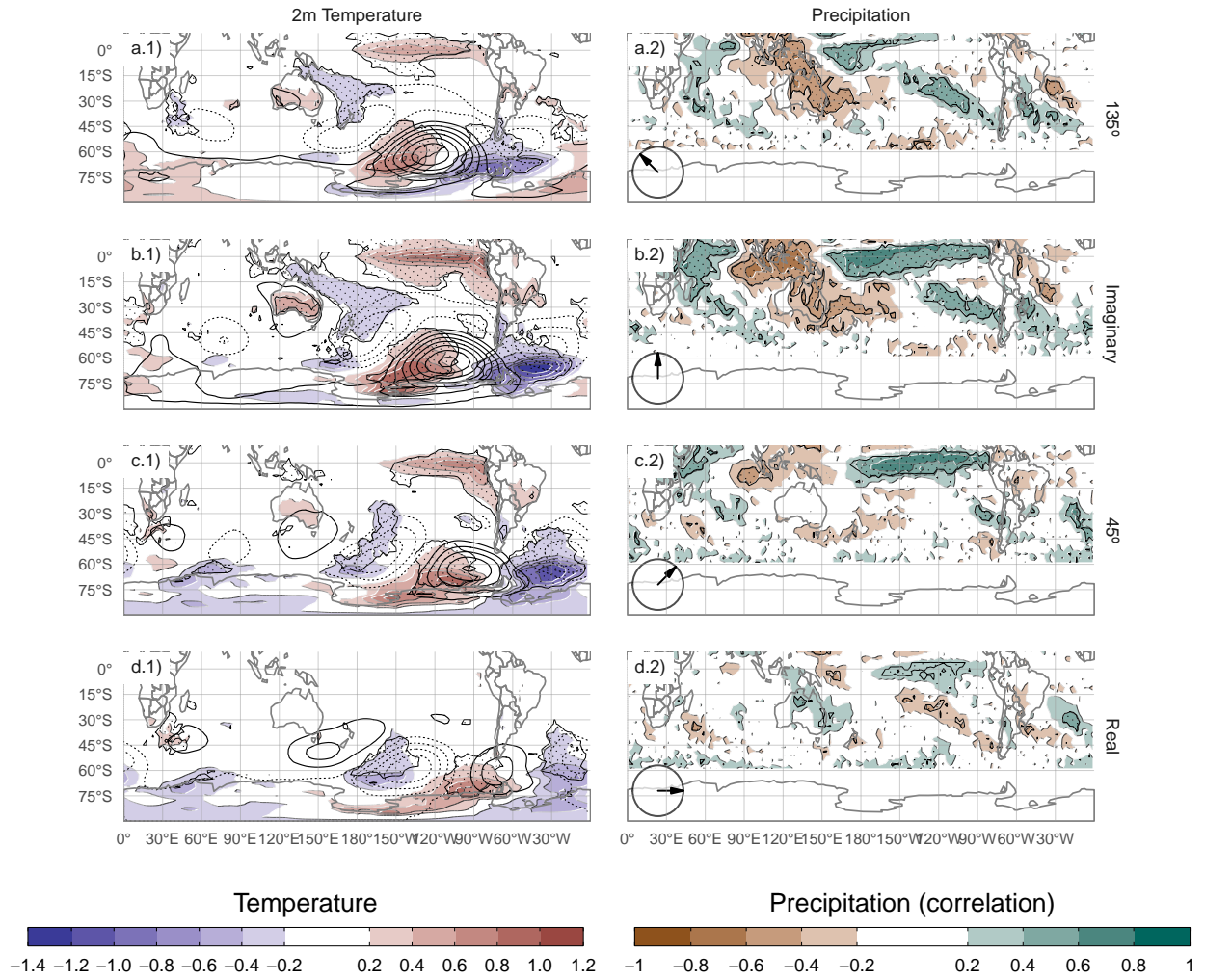


Fig. 14: Regression of SON mean 2-meter temperature (K, shaded) and 850 hPa geopotential height (m, contours) (column 1), and precipitation (correlation, column 2) upon different phases of cEOF2. For the 1979 – 2019. Areas marked with dots have p-values smaller than 0.01 adjusted for False Detection Rate.

Over the continents, the Imaginary cEOF2 (Fig. 14b.1) is associated with positive temperatures in southern Australia and negative temperature in southern South America and the Antarctic Peninsula, that are a result of the wave train described before.

The temperatures anomalies associated with the Real cEOF2 (Fig. 14d.1) are less extensive and restricted to mid and high latitudes.

Over the continents, the temperature anomalies regressions are non significant, except for positive anomalies near the Antarctic Peninsula.

Tropical precipitation anomalies associated with the Imaginary cEOF2 are strong, with positive anomalies in the central Pacific and western Indian, and negative anomalies in the eastern Pacific (Fig. 14b.2). This field is consistent with the SST regression map (Fig. 14b.1) as the positive SST anomalies enhance tropical convection and the negative SST anomalies inhibits it.

In the extra-tropics, the positive Imaginary cEOF2 is related to drier conditions over eastern Australia and the surrounding ocean, that it is similar signal as the one associated with ENSO (Cai et al. 2011). However, the Imaginary cEOF2 is not the direction most correlated with precipitation in that area. The  $135^\circ$  phase (an intermediate between positive Imaginary and negative Real cEOF2) component is associated with stronger and more extensive temporal correlations with precipitation over Australia and New Zealand. The influence of cEOF2 in Australian precipitation could be more related to the direct impacts of SST anomalies in the surrounded oceans rather than on the interconnection pattern represented by the cEOF2.

Over South America, the Imaginary cEOF2 has positive correlations with precipitation in South Eastern South America (SESA) and central Chile, and negative correlations in eastern Brazil. This correlation field matches the springtime precipitation signature of ENSO (e.g. Cai et al. 2020) and it is also similar to the precipitation anomalies associated with the A-SAM (@ Campitelli, Díaz, and Vera 2022).

This result is not surprising considering the close relationship of the Imaginary cEOF2 with both ONI and A-SAM index, which was shown previously. Furthermore, it consolidates the identification of the cEOF2 with the PSA pattern. Resembling the relationship between ONI and the phase of cEOF2 (Fig. 12), there is a cEOF2 phase dependence of the precipitation anomalies in SESA (not shown).

The correlation coefficients between precipitation anomalies and the Real cEOF2 (Fig. 14d.2) are weaker than for Imaginary cEOF2. There is a residual positive correlation in the equatorial eastern Pacific and small, not statistically significant positive correlations over eastern Australia and negative ones over New Zealand.

## 4 Discussion

### discussion

There is some disagreement in the literature of whether the phase of the PSA pattern is affected by the location of tropical SST anomalies (Irving and Simmonds 2016). We show not only that the cEOF2 tends to be in the imaginary phase ( $\sim$ PSA1) when the ENSO region is warm, but that central Pacific SST anomalies tend to move the cEOF towards the negative real phase and eastern Pacific SST anomalies tend to move it towards positive real phase. When ENSO is neutral, the cEOF2 is still as active, but with no preferred phase. This mirrors the results of Cai and Watterson (2002), who showed that the

CSIRO Model can create PSA-like variability even in the absence of ENSO forcing (with a climatological run), but that the variability of one of the PSA modes was enhanced when adding the ENSO signal.

The sensitivity of the phase of the cEOF2 to the location of the tropical SST anomalies was also seen by Ciasto, Simpkins, and England (2015), who detected similar Rossby wave patterns associated with central Pacific and eastern Pacific SST anomalies but with a change in phase.

Some aspects of our work contrast with Irving and Simmonds (2016) analysis of the PSA. They didn't find neither a strong association between PSA-like variability and ENSO, nor a relationship between it and Australian precipitation. Part of the disagreement could be due to the fact that we focus only on SON, which is when the teleconnection pattern is strongest, instead of the whole year. Irving and Simmonds (2016) use of ERA5 forecasted precipitation instead of the more observationally constrained CMAP dataset might also be an issue. But in light of the previous discussion on the importance of the phase of the cEOF2 in its relationship with ENSO and with precipitation impacts, a big difference could be fact that Irving and Simmonds (2016)'s methodology is insensitive to phase changes of the PSA-like variability.

To the extent that the cEOF2 can be identified with the PSA, what is the advantage of the technique proposed here? The spatial fields that the cEOF2 index describes are in quadrature by construction, which makes it possible to derive a proper amplitude and phase. Furthermore, because of the way they are constructed, they are not forced to be orthogonal to the SAM. This allows us to show that Imaginary cEOF2 is closely related to the Southern Annular Mode in the troposphere. In fact, it is so highly correlated to the the zonally asymmetric portion of the SAM that we speculate that that the asymmetric component of the SAM might actually a statistical contamination of the PSA mode.

## 5 Conclusion

conclusion

In this study we assessed the Austral Spring Extratropical Southern Hemisphere zonally asymmetric circulation. For this purpose, two complex indices were derived using Complex Empirical Orthogonal Functions. This allowed us to characterise both the amplitude and phase of planetary waves that are not perfectly organised as sinusoidal waves with constant amplitude at each latitude circle.

The first complex EOF represents the variability of the zonal wave 1 in the stratosphere, but represents a more zonally symmetric monopole in the troposphere. There is a statistically positive trend in the magnitude of this cEOF, which is consistent with previous studies that showed secular changes in springtime wave-1-like patterns (e.g. M. Raphael 2003). This mode is closely related to stratospheric variability such as anomalies in Total Ozone Column. Otherwise, this complex EOF is not related with SST variability and continental precipitation in the Southern Hemisphere.



The second complex EOF represents a wave-3 pattern with maximum magnitude in the Pacific sector. Essentially, it is an alternate representation of the PSA1 and PSA2 patterns (Mo and Paegle 2001). We show that the Imaginary cEOF2 can be roughly identified with the PSA1 and the Real cEOF2 with the PSA2.

The phase of the cEOF2 is related to the the variability of ENSO, but its magnitude appears not to be. Except for the three strongest ENSO events in the period which coincide with the three strongest cEOF2 years.

Precipitation anomalies in South America associated with the Imaginary cEOF2 show a clear ENSO-like impact, with positive anomalies in South-Eastern South America, negative anomalies in Southern Brazil and positive anomalies in central Chile. Precipitation anomalies associated with the Real cEOF2 are low and not statistically significant in this region, showing that the Imaginary phase is optimally aligned with the direction of maximum precipitation impacts there.

On the other hand, over Australia, both the Real and Imaginary phase are associated with significant precipitation anomalies, and we further show that the direction of maximum impact is not aligned with our chosen rotation of cEOF2. An analysis of the precipitation impacts on this regions could benefit for a differnet chosen rotation of the cEOF.

Further work should extend this analysis to other seasons and further study the relationship between the cEOF2 and the SAM. In particular, it is not clear whether the close identification between the Imaginary cEOF2 and the Asymmetric SAM arises from physical processes or statistical contamination.

## Code availability

`code-availability`

A version-controlled repository of the code used to create this analysis, including the code used to download the data can be found at <https://github.com/eliocamp/shceof>.

- The Oceanic Niño Index is available via NOAA’s Climate Prediction Center: [https://www.cpc.ncep.noaa.gov/products/analysis\\_monitoring/ensostuff/detrend.nino34.ascii.txt](https://www.cpc.ncep.noaa.gov/products/analysis_monitoring/ensostuff/detrend.nino34.ascii.txt).
- The Dipole Mode Index is available via Global Climate Observing System Working Group on Surface Pressure: [https://psl.noaa.gov/gcos\\_wgsp/Timeseries/Data/dmi.had.long.data](https://psl.noaa.gov/gcos_wgsp/Timeseries/Data/dmi.had.long.data)

## A Extra figures

`extra-figures`

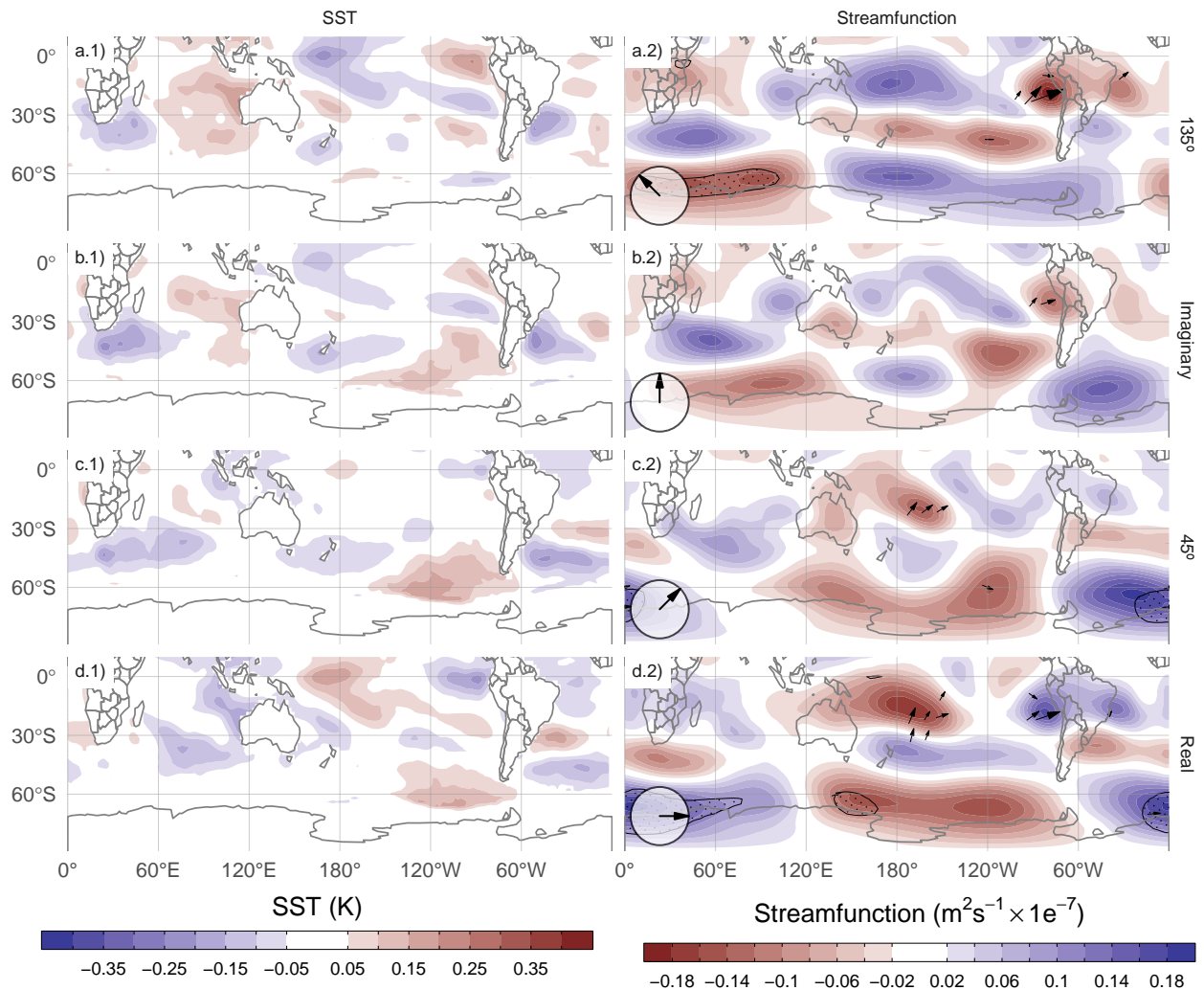


Fig. A.1: Same as Figure 11 but for cEOF1.

fig:sst-psi-1

- Adams, John C., Paul N. Swartztrauber, and Roland Sweet. 1999. "FISHPACK, a Package of Fortran Subprograms for the Solution of Separable Elliptic Partial Differential Equations." 1999. <https://www2.cisl.ucar.edu/resources/legacy/fishpack>.
- Albers, Sam, and Elio Campitelli. 2020. *Rsoi: Import Various Northern and Southern Hemisphere Climate Indices* (version 0.5.4). <https://CRAN.R-project.org/package=rsoi>.
- Allaire, J. J., Yihui Xie [aut, cre, Jonathan McPherson, Javier Luraschi, Kevin Ushey, Aron Atkins, et al. 2020. *Rmarkdown: Dynamic Documents for R* (version 2.4). <https://CRAN.R-project.org/package=rmarkdown>.
- Baldwin, Mark P., and David W. J. Thompson. 2009. "A Critical Comparison of Stratosphere-Troposphere Coupling Indices." *Quarterly Journal of the Royal Meteorological Society* 135 (644): 1661–72. <https://doi.org/10.1002/qj.479>.

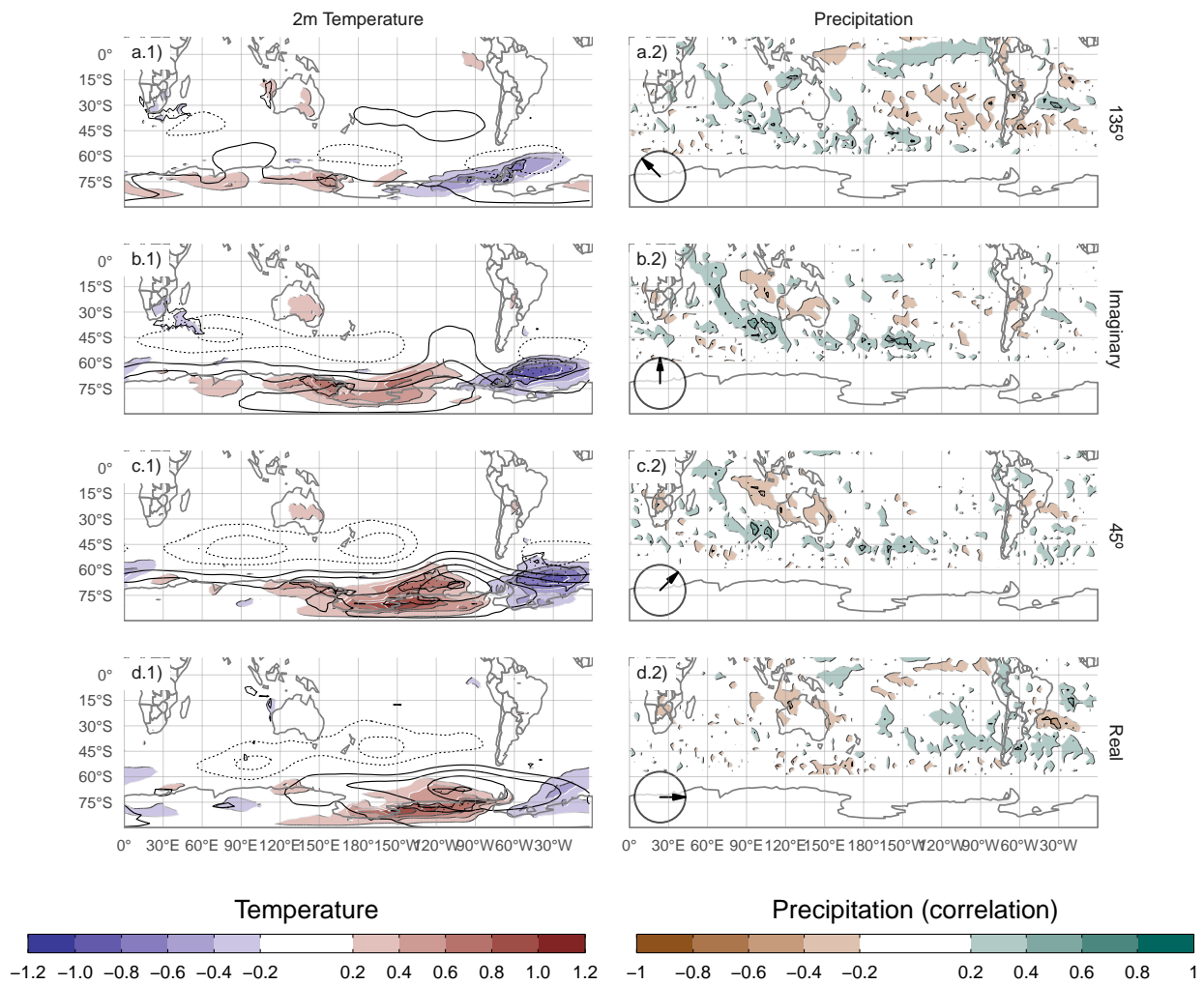


Fig. A.2: Same as Figure 14 but for cEOF1.

- Bamston, Anthony G., Muthuvel Chelliah, and Stanley B. Goldenberg. 1997. "Documentation of a Highly ENSO-related Sst Region in the Equatorial Pacific: Research Note." *Atmosphere-Ocean* 35 (3): 367–83. <https://doi.org/10.1080/07055900.1997.9649597>.
- Bell, B., H. Hersbach, P. Berrisford, P. Dahlgren, A. Horányi, J. Muñoz Sabater, J. Nicolas, et al. 2020. "Era5 Monthly Averaged Data on Pressure Levels from 1950 to 1978 (Preliminary Version)." *Copernicus Climate Change Service (C3s) Climate Data Store (CDS)* (Accessed on <26-08-2021>), <https://cds.climate.copernicus.eu/cdsapp#!/dataset/reanalysis-era5-pressure-levels-monthly-means-preliminary-back-extension?tab=overview>.
- Benjamini, Yoav, and Yosef Hochberg. 1995. "Controlling the False Discovery Rate: A Practical and Powerful Approach to Multiple Testing." *Journal of the Royal Statistical Society: Series B (Methodological)* 57 (1): 289–300. <https://doi.org/10.1111/j.2517-6161.1995.tb02031.x>.

- Cai, Wenju, Michael J. McPhaden, Alice M. Grimm, Regina R. Rodrigues, Andréa S. Taschetto, René D. Garreaud, Boris Dewitte, et al. 2020. "Climate Impacts of the El Niño–Southern Oscillation on South America." *Nature Reviews Earth & Environment* 1 (4, 4): 215–31. <https://doi.org/10.1038/s43017-020-0040-3>.
- Cai, Wenju, Peter van Rensch, Tim Cowan, and Harry H. Hendon. 2011. "Teleconnection Pathways of ENSO and the IOD and the Mechanisms for Impacts on Australian Rainfall." *Journal of Climate* 24 (15): 3910–23. <https://doi.org/10.1175/2011JCLI4129.1>.
- Cai, Wenju, and Ian G. Watterson. 2002. "Modes of Interannual Variability of the Southern Hemisphere Circulation Simulated by the CSIRO Climate Model." *Journal of Climate* 15 (10): 1159–74. [https://doi.org/10.1175/1520-0442\(2002\)015%3C1159:M0IV0T%3E2.0.CO;2](https://doi.org/10.1175/1520-0442(2002)015%3C1159:M0IV0T%3E2.0.CO;2).
- Campitelli, Elio. 2020. *metR: Tools for Easier Analysis of Meteorological Fields* (version 0.7.0). <https://CRAN.R-project.org/package=metR>.
- Campitelli, Elio, Leandro B. Díaz, and Carolina Vera. 2022. "Assessment of Zonally Symmetric and Asymmetric Components of the Southern Annular Mode Using a Novel Approach." *Climate Dynamics* 58 (1): 161–78. <https://doi.org/10.1007/s00382-021-05896-5>.
- Cazes-Boezio, Gabriel, Andrew W. Robertson, and Carlos R. Mechoso. 2003. "Seasonal Dependence of ENSO Teleconnections over South America and Relationships with Precipitation in Uruguay." *Journal of Climate* 16 (8): 1159–76. [https://doi.org/10.1175/1520-0442\(2003\)16%3C1159:SDOET0%3E2.0.CO;2](https://doi.org/10.1175/1520-0442(2003)16%3C1159:SDOET0%3E2.0.CO;2).
- Ciasto, Laura M., Graham R. Simpkins, and Matthew H. England. 2015. "Teleconnections Between Tropical Pacific SST Anomalies and Extratropical Southern Hemisphere Climate." *Journal of Climate* 28 (1): 56–65. <https://doi.org/10.1175/JCLI-D-14-00438.1>.
- Dowle, Matt, and Arun Srinivasan. 2020. *Data.table: Extension of 'Data.frame'* (version 1.13.0). <https://CRAN.R-project.org/package=data.table>.
- Fogt, Ryan L., and Gareth J. Marshall. 2020. "The Southern Annular Mode: Variability, Trends, and Climate Impacts Across the Southern Hemisphere." *WIREs Climate Change* 11 (4): e652. <https://doi.org/10.1002/wcc.652>.
- Gelbrecht, Maximilian, Niklas Boers, and Jürgen Kurths. 2018. "Phase Coherence Between Precipitation in South America and Rossby Waves." *Science Advances* 4 (12): eaau3191. <https://doi.org/10.1126/sciadv.aau3191>.
- Gong, Daoyi, and Shaowu Wang. 1999. "Definition of Antarctic Oscillation Index." *Geophysical Research Letters* 26 (4): 459–62. <https://doi.org/10.1029/1999GL900003>.
- Grytsai, A. 2011. "Planetary Wave Peculiarities in Antarctic Ozone Distribution During 1979–2008." *International Journal of Remote Sensing* 32 (11): 3139–51. <https://doi.org/10.1080/01431161.2010.541518>.
- Hartmann, Dennis L., and Rolando R. Garcia. 1979. "A Mechanistic Model of Ozone Transport by Planetary Waves in the Stratosphere." *Journal of the Atmospheric Sciences* 36 (2): 350–64. [https://doi.org/10.1175/1520-0469\(1979\)036%3C0350:AMM00T%3E2.0.CO;2](https://doi.org/10.1175/1520-0469(1979)036%3C0350:AMM00T%3E2.0.CO;2).
- Hersbach, H., B. Bell, P. Berrisford, G. Biavati, A. Horányi, J. Muñoz Sabater, J. Nicolas, et al. 2019. "Era5 Monthly Averaged Data on Pressure Levels from 1979 to Present." *Copernicus Climate Change Service (C3s) Climate Data Store (CDS)* (Accessed on <07-09-2021>). <https://doi.org/10.24381/cds.6860a573>.
- Hobbs, William R., and Marilyn N. Raphael. 2010. "Characterizing the Zonally Asymmetric Component of the SH Circulation." *Climate Dynamics* 35 (5): 859–73. <https://doi.org/10.1007/s00382-009-0663-z>.
- Horel, J. D. 1984. "Complex Principal Component Analysis: Theory and Examples." *Journal of Applied Meteorology and Climatology* 23 (12): 1660–73. [https://doi.org/10.1175/1520-0450\(1984\)023%3C1660:CPCATA%3E2.0.CO;2](https://doi.org/10.1175/1520-0450(1984)023%3C1660:CPCATA%3E2.0.CO;2).
- Hoskins, B. J., and K. I. Hodges. 2005. "A New Perspective on Southern Hemisphere Storm Tracks." *Journal of Climate* 18 (20): 4108–29. <https://doi.org/10.1175/JCLI3570.1>.
- Huang, Boyin, Peter W. Thorne, Viva F. Banzon, Tim Boyer, Gennady Chepurin, Jay H. Lawrimore, Matthew J. Menne, Thomas M. Smith, Russell S. Vose, and Huai-Min Zhang. 2017. "Extended Reconstructed Sea Surface Temperature, Version 5 (ERSSTv5):

- Upgrades, Validations, and Intercomparisons." *Journal of Climate* 30 (20): 8179–8205. <https://doi.org/10.1175/JCLI-D-16-0836.1>.
- Hufkens, Koen. 2020. *Ecmwfr: Programmatic Interface to the Two European Centre for Medium-Range Weather Forecasts API Services* (version 1.3.0). <http://doi.org/10.5281/zenodo.2647541>.
- Irving, Damien, and Ian Simmonds. 2015. "A Novel Approach to Diagnosing Southern Hemisphere Planetary Wave Activity and Its Influence on Regional Climate Variability." *Journal of Climate* 28 (23): 9041–57. <https://doi.org/10.1175/JCLI-D-15-0287.1>.
- . 2016. "A New Method for Identifying the Pacific–South American Pattern and Its Influence on Regional Climate Variability." *Journal of Climate* 29 (17): 6109–25. <https://doi.org/10.1175/JCLI-D-15-0843.1>.
- Kao, Hsun-Ying, and Jin-Yi Yu. 2009. "Contrasting Eastern-Pacific and Central-Pacific Types of ENSO." *Journal of Climate* 22 (3): 615–32. <https://doi.org/10.1175/2008JCLI2309.1>.
- Katz, Richard W., and Barbara G. Brown. 1991. "The Problem of Multiplicity in Research on Teleconnections." *International Journal of Climatology* 11 (5): 505–13. <https://doi.org/10.1002/joc.3370110504>.
- Krokhin, V. V., and W. M. J. Luxemburg. 2007. "Temperatures and Precipitation Totals over the Russian Far East and Eastern Siberia: Long-Term Variability and Its Links to Teleconnection Indices." *Hydrology and Earth System Sciences* 11 (6): 1831–41. <https://doi.org/10.5194/hess-11-1831-2007>.
- Lim, E.-P., H. H. Hendon, and D. W. J. Thompson. 2018. "Seasonal Evolution of Stratosphere–Troposphere Coupling in the Southern Hemisphere and Implications for the Predictability of Surface Climate." *Journal of Geophysical Research: Atmospheres* 123 (21): 12,002–12,016. <https://doi.org/10.1029/2018JD029321>.
- Loon, Harry van, and Roy L. Jenne. 1972. "The Zonal Harmonic Standing Waves in the Southern Hemisphere." *Journal of Geophysical Research* 77 (6): 992–1003. <https://doi.org/10.1029/JC077i006p00992>.
- Mo, Kingtse C. 2000. "Relationships Between Low-Frequency Variability in the Southern Hemisphere and Sea Surface Temperature Anomalies." *Journal of Climate* 13 (20): 3599–3610. [https://doi.org/10.1175/1520-0442\(2000\)013%3C3599:RBLFVI%3E2.0.CO;2](https://doi.org/10.1175/1520-0442(2000)013%3C3599:RBLFVI%3E2.0.CO;2).
- Mo, Kingtse C., and Julia N. Paegle. 2001. "The Pacific–South American Modes and Their Downstream Effects." *International Journal of Climatology* 21 (10): 1211–29. <https://doi.org/10.1002/joc.685>.
- Nuncio, M., and Xiaojun Yuan. 2015. "The Influence of the Indian Ocean Dipole on Antarctic Sea Ice." *Journal of Climate* 28 (7): 2682–90. <https://doi.org/10.1175/JCLI-D-14-00390.1>.
- Pezza, Alexandre Bernardes, Harun A. Rashid, and Ian Simmonds. 2012. "Climate Links and Recent Extremes in Antarctic Sea Ice, High-Latitude Cyclones, Southern Annular Mode and ENSO." *Climate Dynamics* 38 (1): 57–73. <https://doi.org/10.1007/s00382-011-1044-y>.
- Plumb, R. Alan. 1985. "On the Three-Dimensional Propagation of Stationary Waves." *Journal of the Atmospheric Sciences* 42 (3): 217–29. [https://doi.org/10.1175/1520-0469\(1985\)042%3C0217:OTTDPO%3E2.0.CO;2](https://doi.org/10.1175/1520-0469(1985)042%3C0217:OTTDPO%3E2.0.CO;2).
- R Core Team. 2020. *R: A Language and Environment for Statistical Computing*. Manual. Vienna, Austria: R Foundation for Statistical Computing. <https://www.R-project.org/>.
- Raphael, M. N. 2004. "A Zonal Wave 3 Index for the Southern Hemisphere." *Geophysical Research Letters* 31 (23). <https://doi.org/10.1029/2004GL020365>.
- . 2007. "The Influence of Atmospheric Zonal Wave Three on Antarctic Sea Ice Variability." *Journal of Geophysical Research: Atmospheres* 112 (D12). <https://doi.org/10.1029/2006JD007852>.
- Raphael, Marilyn. 2003. "Recent, Large-Scale Changes in the Extratropical Southern Hemisphere Atmospheric Circulation." *Journal of Climate* 16 (17): 2915–24. [https://doi.org/10.1175/1520-0442\(2003\)016%3C2915:RLCITE%3E2.0.CO;2](https://doi.org/10.1175/1520-0442(2003)016%3C2915:RLCITE%3E2.0.CO;2).
- Saji, N. H., B. N. Goswami, P. N. Vinayachandran, and T. Yamagata. 1999. "A Dipole Mode in the Tropical Indian Ocean." *Nature* 401 (6751, 6751): 360–63. <https://doi.org/10.1038/43854>.

- Saji, N. H., and T. Yamagata. 2003. "Possible Impacts of Indian Ocean Dipole Mode Events on Global Climate." *Climate Research* 25 (2): 151–69. <https://doi.org/10.3354/cr025151>.
- Smith, Anne K. 1995. "Numerical Simulation of Global Variations of Temperature, Ozone, and Trace Species in the Stratosphere." *Journal of Geophysical Research: Atmospheres* 100 (D1): 1253–69. <https://doi.org/10.1029/94JD02395>.
- Trenberth, Kevin E. 1980. "Planetary Waves at 500 Mb in the Southern Hemisphere." *Monthly Weather Review* 108 (9): 1378–89. [https://doi.org/10.1175/1520-0493\(1980\)108%3C1378:PWAMIT%3E2.0.CO;2](https://doi.org/10.1175/1520-0493(1980)108%3C1378:PWAMIT%3E2.0.CO;2).
- Trenberth, Kevin F., and K. C. Mo. 1985. "Blocking in the Southern Hemisphere." *Monthly Weather Review* 113 (1): 3–21. [https://doi.org/10.1175/1520-0493\(1985\)113%3C0003:BITSH%3E2.0.CO;2](https://doi.org/10.1175/1520-0493(1985)113%3C0003:BITSH%3E2.0.CO;2).
- Turner, John, J. Scott Hosking, Thomas J. Bracegirdle, Tony Phillips, and Gareth J. Marshall. 2017. "Variability and Trends in the Southern Hemisphere High Latitude, Quasi-Stationary Planetary Waves." *International Journal of Climatology* 37 (5): 2325–36. <https://doi.org/10.1002/joc.4848>.
- Walker, Sir Gilbert Thomas. 1914. *Correlation in Seasonal Variations of Weather, III: On the Criterion for the Reality of Relationships Or Periodicities*. Meteorological Office. <https://books.google.com?id=cuGtuAAACAAJ>.
- Wickham, Hadley. 2009. *Ggplot2: Elegant Graphics for Data Analysis*. Use R! New York: Springer-Verlag. <https://doi.org/10.1007/978-0-387-98141-3>.
- Wilks, D. S. 2016. "'The Stippling Shows Statistically Significant Grid Points': How Research Results Are Routinely Overstated and Overinterpreted, and What to Do about It." *Bulletin of the American Meteorological Society* 97 (12): 2263–73. <https://doi.org/10.1175/BAMS-D-15-00267.1>.
- Wilks, Daniel. 2011. *Statistical Methods in the Atmospheric Sciences*. Vol. 100. Elsevier. <https://doi.org/10.1016/B978-0-12-385022-5.00022-1>.
- Wirth, Volkmar. 1993. "Quasi-Stationary Planetary Waves in Total Ozone and Their Correlation with Lower Stratospheric Temperature." *Journal of Geophysical Research: Atmospheres* 98 (D5): 8873–82. <https://doi.org/10.1029/92JD02820>.
- Xie, Pingping, and Phillip A. Arkin. 1997. "Global Precipitation: A 17-Year Monthly Analysis Based on Gauge Observations, Satellite Estimates, and Numerical Model Outputs." *Bull. Amer. Meteor. Soc.* 78 (Accessed on <26-08-2021>) (11): 2539–58. [https://doi.org/10.1175/1520-0477\(1997\)078%3C2539:GPAYMA%3E2.0.CO;2](https://doi.org/10.1175/1520-0477(1997)078%3C2539:GPAYMA%3E2.0.CO;2).
- Xie, Yihui. 2015. *Dynamic Documents with R and Knitr*. 2nd ed. Boca Raton, Florida: Chapman and Hall/CRC. <https://yihui.org/knitr/>.